

Similarity simulation of fractal features in embankment slope failure based on acoustic emission detection

This paper aims at making accurate prediction of embankment slope failures. To this end, the acoustic emission(AE) technique is introduced to monitor the slope stability of embankments, and the similarity simulation is carried out indoor on embankment slopes with waveguide rods of different diameters and gravels with distinctive particle sizes. In the simulation tests, the AE feature data of the embankment slope models are obtained during the failure process. Then, the fractal theory is applied to analyse the features and variation patterns of the AE energy fractal dimensions of the embankment slopes throughout the failure process. The author also analyses the features and variation patterns of AE energy fractal dimension during embankment slope failure. The test results show that the fractal dimension remained at a low level at the onset, continued to increase during the test, and eventually peaked at the middle phase of the test. In the final phase, the fractal dimension started to decrease. The AE fractal dimension also peaked at the slip-impending phase and then drop all of a sudden. This research offers a valuable detection means for the forecast of embankment slope failure.

Keywords: Acoustic emission (AE), embankment slope, fractal dimension, similarity simulation.

1. Introduction

The stability monitoring and failure prediction of slope embankment have long been an important part of highway construction and operation in mountainous regions [1-4]. This is particularly true in China, a country known for its complicated geology and the frequent occurrence of landslide and other disasters. As a result, a variety of technologies have been developed for slope deformation monitoring in China, such as inclinometer, optical

fibre sensor network and so on. Using the inclinometer, the deformation monitoring requires the regular presence of workers at the site for data collection. Thus, this traditional method is featured by heavy workload, low automation and delays in monitoring. As for the optical fibre sensor network, the monitoring process is of relatively high cost, in spite of the high sensitivity, accuracy and instantaneity. The acoustic emission (AE)-based embankment slope monitoring overcomes the defects of these common strategies and achieves high automation and real-time monitoring ability at a low cost [5-6]. Many previous studies have shown the effectiveness of applying the AE for slope stability monitoring and the fractal theory for AE parameter calculation [7-8]. However, there is rarely any report on the application of the fractal theory in the research on AE parameters of embankment slope failure.

In view of the above, this paper examines the AE parameters of embankment slope failure and introduces the fractal theory, e.g. fractal dimension, to depict the AE energy [9-12]. Furthermore, similarity simulation of embankment slope failure was conducted indoor using rock-soil mass of an embankment slope as simulation materials. The AE features of embankment slopes with known sliding surface were discussed under the controlled conditions of waveguide rods of different diameters and gravels with distinctive particle sizes. Through the simulation and discussion, the authors proposed a AE-based prediction method for embankment slope failure.

2. Similarity simulation

2.1 TEST SET UP AND MODEL

The simulation tests use a PCI-II AEwin™ AE system (PAC) (Fig.1), one of the best and most popular of its kind. The waveguide rods are 1m in length, and 14mm, 18mm and 22mm in diameter, respectively. Two waveguide rods were provided for each diameter. The particle size of the gravels is 5~10mm, 10~16mm and 16~20mm, respectively. Therefore, the waveguide rods and gravels can be combined in 9 different

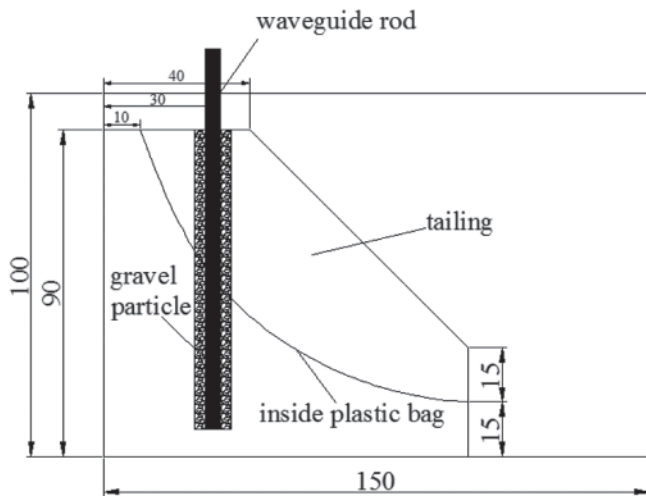
Messrs. Wen Zhong, Fucan Yue, Daohuan Zha, Chunsheng Li, Yunchuan Deng and Xin Chen, School of Resources and Environment Engineering and Mr. Wen Zhong, Jiangxi Key Laboratory of Mining Engineering, Jiangxi University of Science and Technology, Ganzhou Jiangxi 341 000, China. E-mail:vincezone@163.com

ways depending on the rod diameter and particle size.

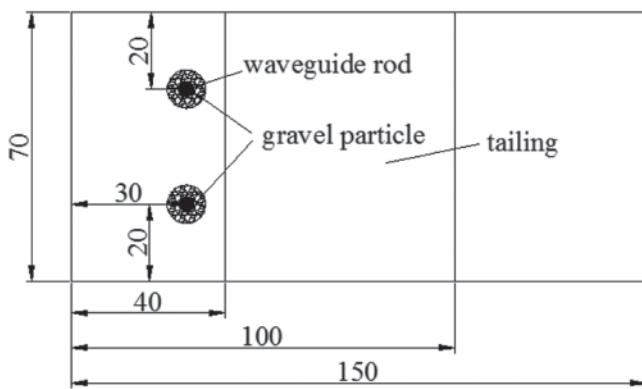


Fig.1 PCI-II AE system

The simulation materials are rock-soil mass collected from an embankment slope. The rock-soil mass models are 1.5m×0.7m×1.0m (L×W×H) and 45° in slope. Each model was divided into the sliding mass in the upper part and the fixed part in the lower part by the known sliding surface. Fig.2 specifies the dimensions of the model. The known sliding



(a) Elevation view



(b) Plan view

Fig.2 Test model

surface was simulated by a plastic bag of thin film. In the test, the plastic bag was filled with water to simulate the embankment slope failure.

2.2 TEST PLAN

As shown in Fig.2, gravels of different particle sizes are arranged around the waveguide rods. The 9 combinations of rods and gravels are each tested four times. When water is injected into the known sliding surface, the AE failure monitoring is conducted on the model in real-time. In this way, the AE feature parameters of the embankment are captured for each combination.

2.3 TEST RESULTS ANALYSIS

The failure process of the model can be divided into four stages: micro-cracking, crack propagation, slip-impending and sliding failure (Fig.3). Figs.4 and 5 respectively illustrate the AE event rate and the AE energy rate curve of the model with rod diameter of 14mm and gravel particle size of 16~20mm.

Despite the differences in rod diameter and gravel particle size, the test models shared basically the same AE event rate



(a) Micro-cracking

(b) Crack propagation



(c) Slip-impending

(d) Sliding failure

Fig.3 Failure process

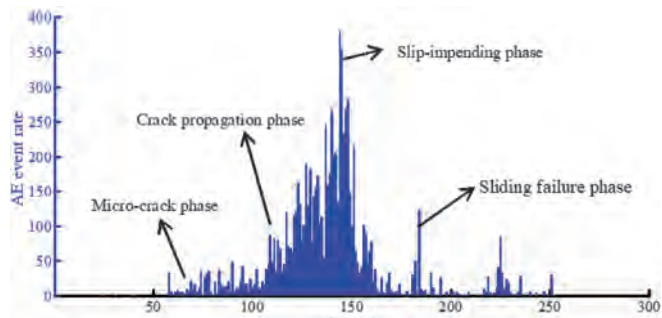


Fig.4 Cavity geometry (waveguide rod diameter 14mm, gravel particle diameter 16~20mm)

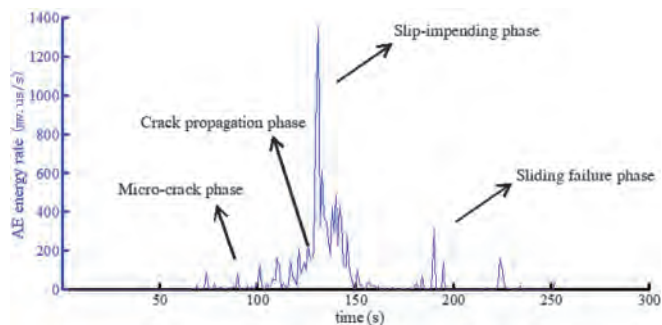
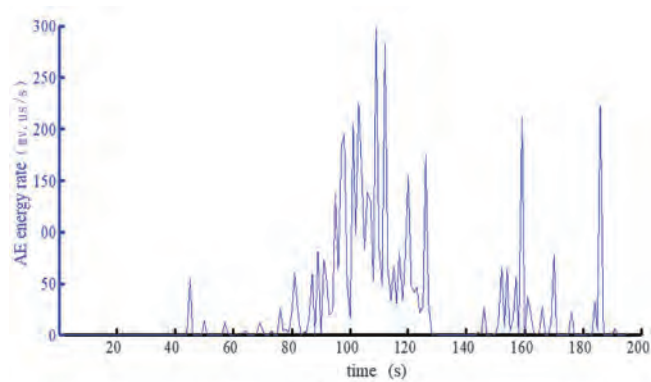


Fig.5 AE energy rate curve (waveguide rod diameter 14mm, gravel particle diameter 16~20mm)

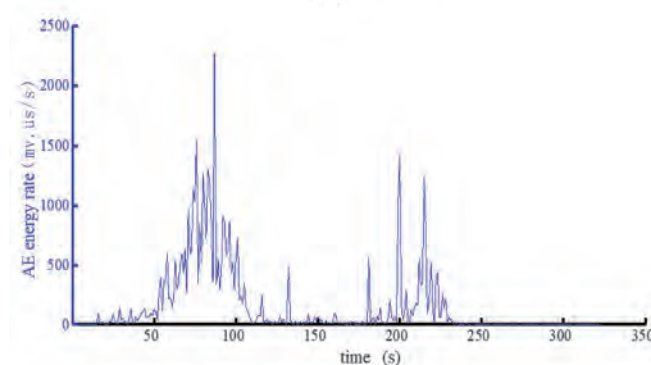
curves and only differed in some local areas. The general trend is described as follows. In the micro-cracking phase, the AE activities are negligible, and the mean AE event rate is relatively small. As the microcracks expanded into macrocracks, the AE activities are much more active. In this case, the AE event rate picked up speed and possessed a greater mean value. In the slip-impeding phase, the AE activities became so intense that the AE event rate soared to the maximum mean value. The final phase of sliding failure witnesses relatively mild AE activities, and a drastic decrease in the AE event rate, thus a smaller mean value.

Figs.6~8 present the AE energy rate curves of the nine combinations. It can be seen that the AE energy rate changed in a similar pattern despite the variation in particle size. In other words, the energy rate is continuously increasing in the micro-cracking and crack propagation phases, peaked in the slip-impeding phase, and decreased again in the sliding failure phase.

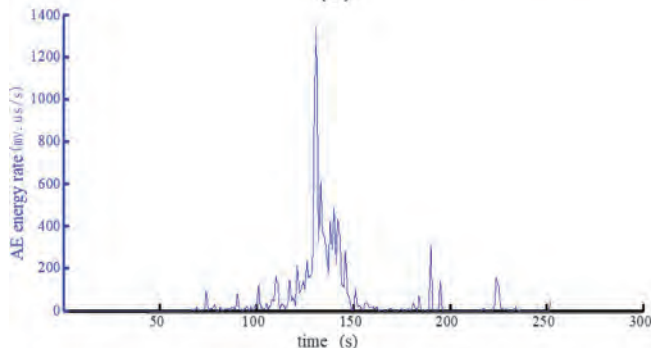
The simulation tests reveal that the AE energy rate and AE event rate borne high resemblance to each other in the sliding failure phase. Comparing the values of AE energy rates, it is learned that the slip-impeding phase had a greater AE energy rate than the other phases, indicating that the micro-cracks propagated continuously to a macro-scale failing surface in this phase. During this period, the AE intensity is far greater than that in the other three phases, and the value of AE energy rate depended on the gravel particle size. The energy rate always reached its peak in this phase,



(a)



(b)



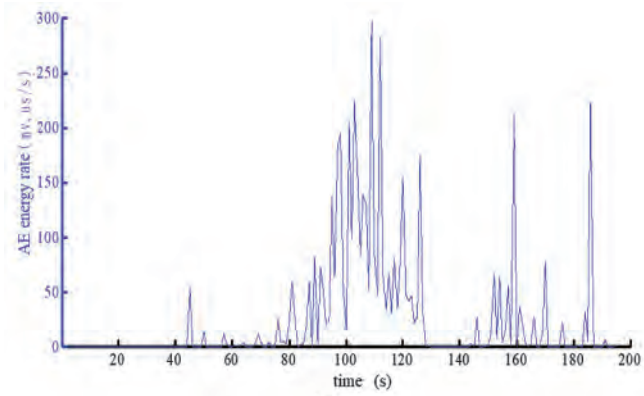
(c)

Fig.6 The curve of AE energy rate (waveguide rod diameter: 14mm)

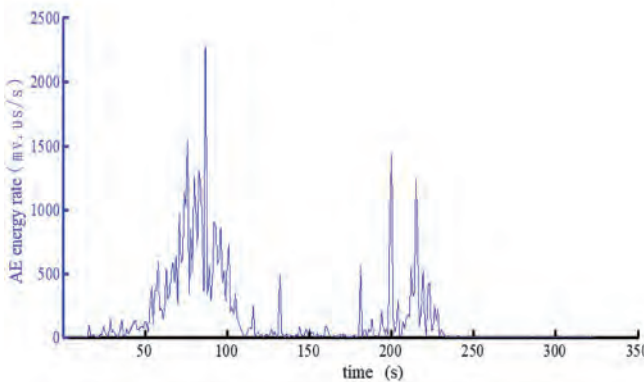
no matter how large is the diameter of the waveguide rods. The gravel particle sizes are ranked as 10~16mm, 16~20mm and 5~10mm in descending order of the peak value. Meanwhile, combinations of the 10~16mm gravel boasted the largest mean value.

3. Fractal dimension calculation

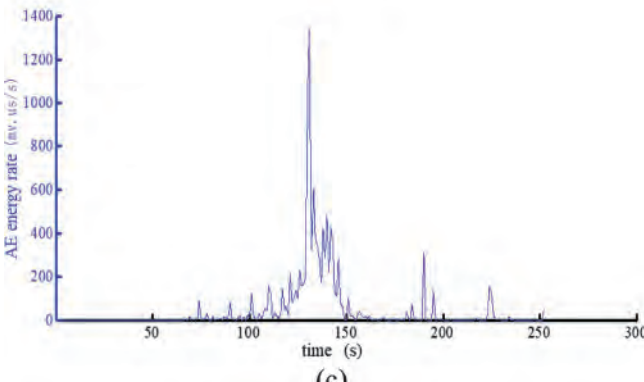
For an AE sequence, a statistical curve (e.g. AE energy rate, AE event rate) can be obtained through the correlation analysis of some response features of the rock-soil mass during the failure process. Nevertheless, the numerical value (e.g. energy, range) of a single AE parameter often varies disorderly with respect to time [13-14]. The irregular and chaotic value can be well depicted by fractals, an indicator of the local features (e.g. morphology, function and space-time)



(a)



(b)



(c)

Fig.7 The curve of AE energy rate (waveguide rod diameter: 18mm)

of things that are similar in some ways to the global features. The previous research has shown that the physical mechanical behaviours of geomaterials, namely deformation, failure and dissipation, are fractal in nature [15-16]. The centrepiece of the fractal theory lies in the calculation of fractal dimension. The increase of fractal dimension means an event is progressing to the chaotic state, while the decrease of fractal dimension reveals the opposite trend [17].

For a sample with a capacity of n , the AE energy time series is:

$$\dots \quad (1)$$

$N(N = n-m+1)m$ vector could be constructed:

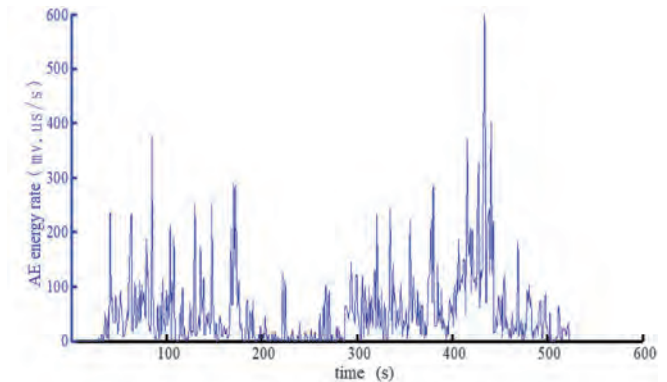
$$\dots \quad (2)$$

In a given dimension:

$$r(k) = k \frac{i}{N^2} \sum_{i=1}^N \sum_{j=1}^N |X_i - X_j| \quad \dots \quad (3)$$

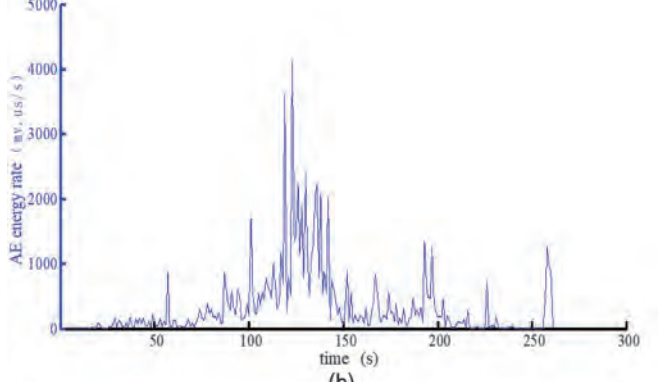
where k is a proportional constant ranging between 10 and 20.

The associated function $W[r(k)]$ of each vector can be expressed as:

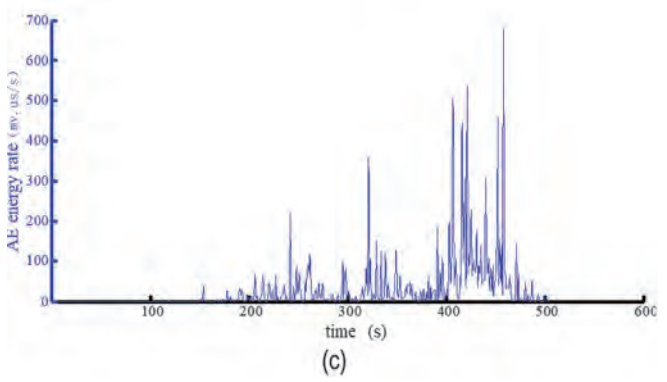


(a)

X



(b)



(c)

Fig.8 The curve of AE energy rate (waveguide rod diameter: 22mm)

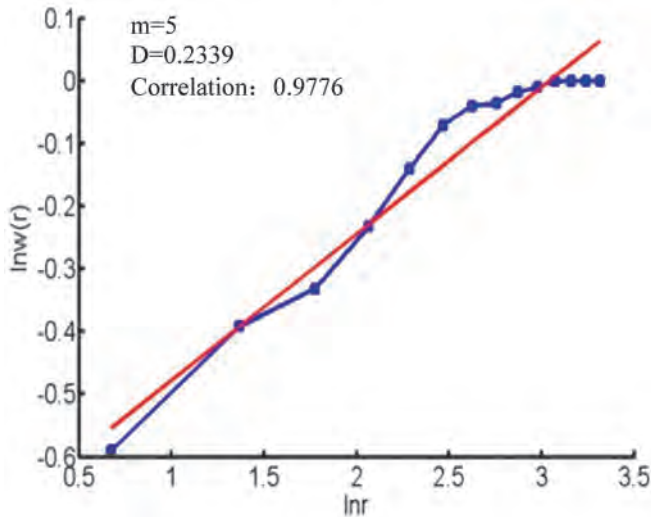


Fig.9 $Inr(k)-InW[r(k)]$ curve

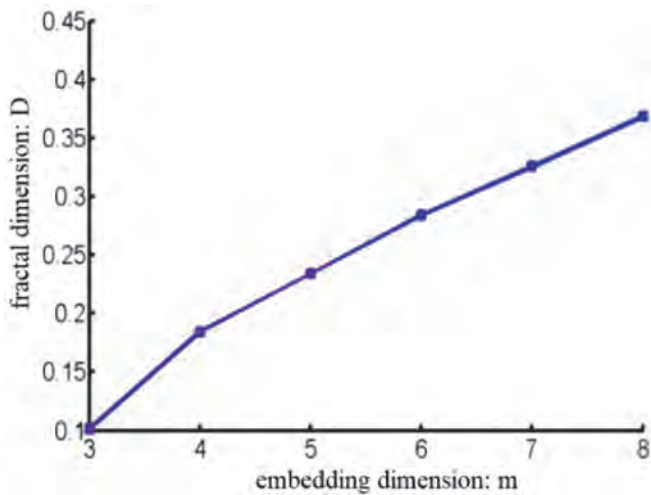
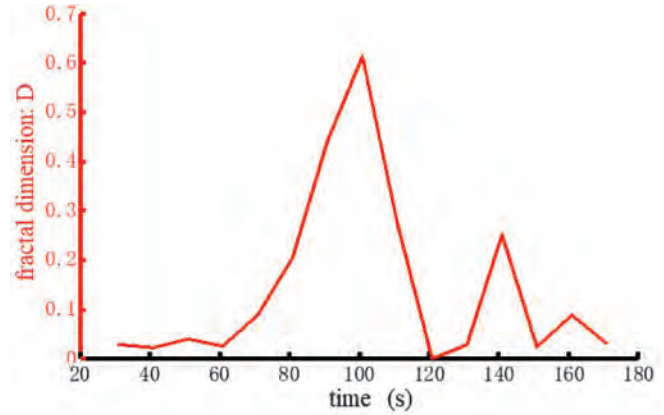


Fig.10 Embedding dimension-fractal dimension curve

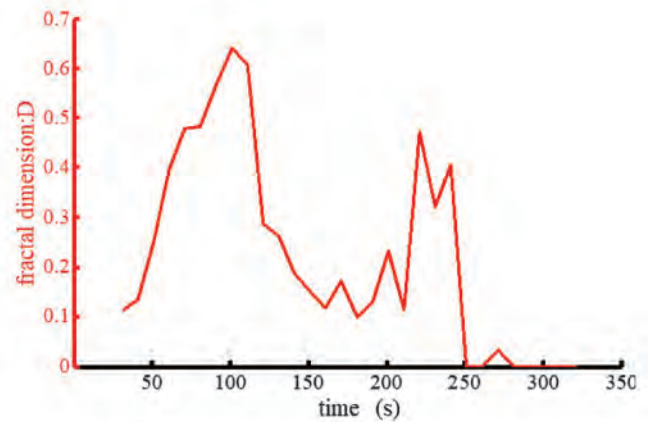
$$W[r(k)] = \frac{1}{N^2} \sum_{i=1}^N \sum_{j=1}^N H[r(k) - |X_i - X_j|] \quad \dots \quad (4)$$

where H is the heaviside step function.

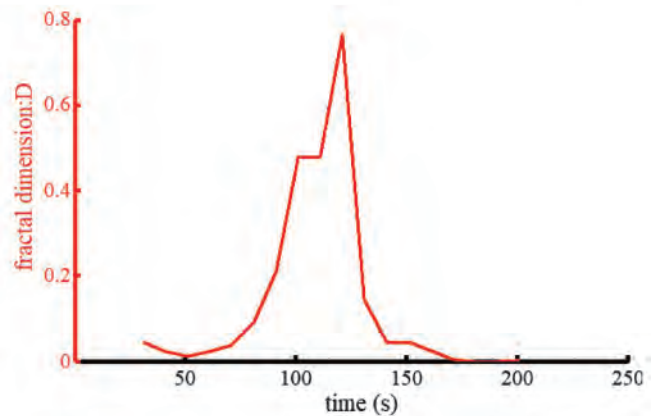
Then, at given g scales, g points can be obtained with coordinates $\{Inr(k), InW[r(k)]\}$. If these points fall on a straight line, the AE energy sequence can be considered as having fractal features, and the slope of the straight line can be deemed as the associated dimension D of AE energy. From Equation (2), the embedding dimension m directly hinges on the fractal dimension D . Fig.9 shows that the $Inr(k) - InW[r(k)]$ curve of an AE energy sequence with a sample size of 1,000 at embedding dimension $m = 5$. It is clear that the curve is approximately a straight line, indicating that the AE energy sequence of the embankment model has fractal features. It can be seen from Fig.10 that the fractal dimension increases in a stepwise manner at an embedding dimension greater than 4. Hence, the value of m is set to 5.



(a) Diameter: 5-10mm



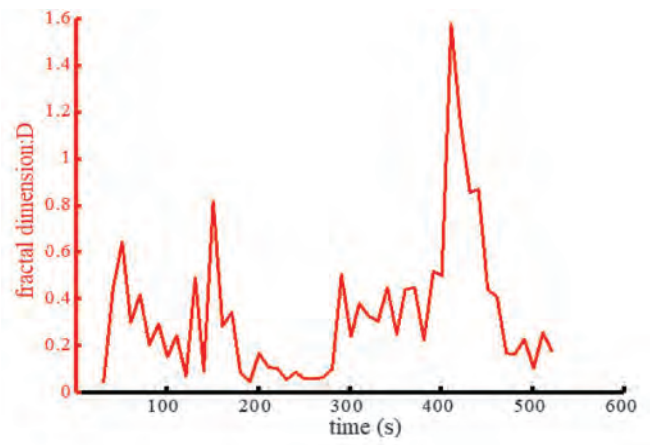
(b) Diameter: 10-16mm



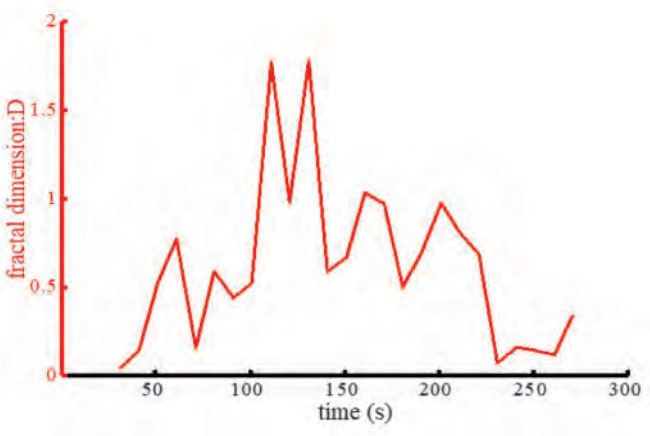
(c) Diameter: 16-20mm

Fig.11 AE energy fractal dimension curves of combinations with 14mm-diameter waveguide rod

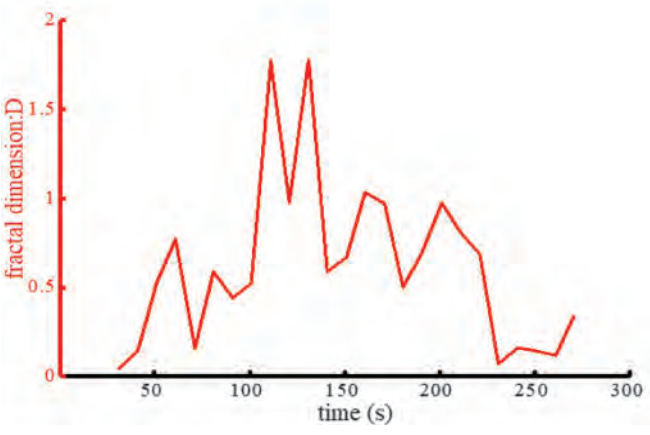
To save time, only 1,000 AE energy data are selected to calculate a fractal dimension. Since the AE number produced during the sliding failure of embankment slopes cannot be divided by 1,000 without a remainder, the truncation effect is bound to occur when 1,000 is taken as the sample capacity of a fractal dimension. Through the discussion of the AE energy, it can be seen that the AE energy increased obviously with



(a) Diameter: 5-10mm

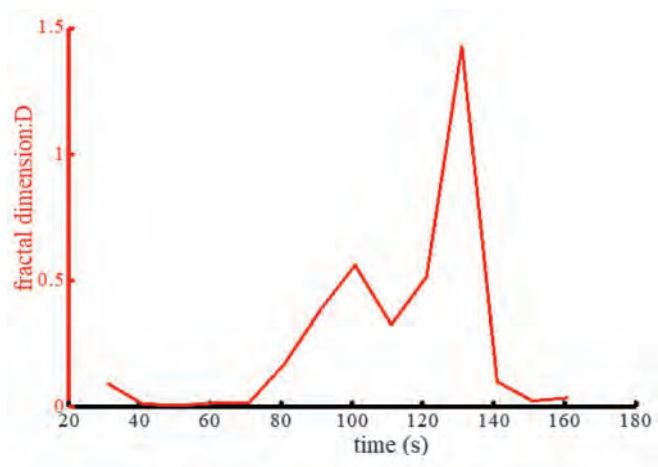


(b) Diameter: 10-16mm

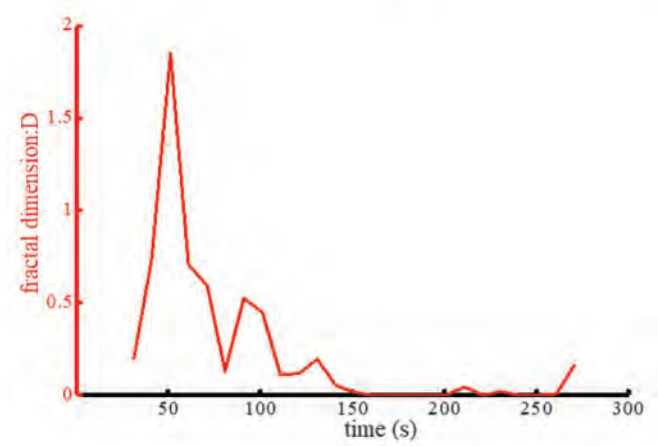


(c) Diameter: 16-20mm

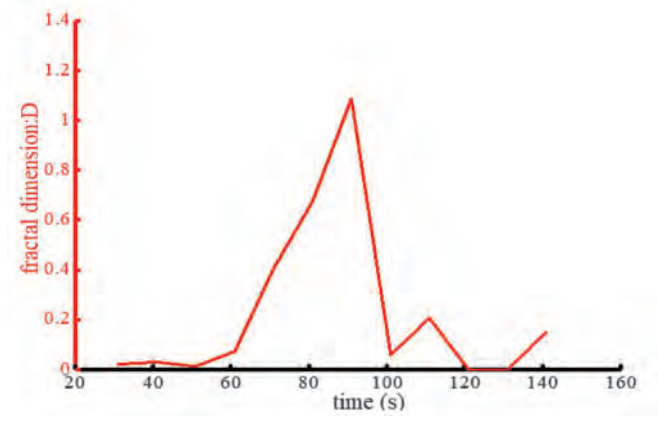
Fig.12 AE energy fractal dimension curves of combinations with 18mm-diameter waveguide rod



(a) Diameter: 5-10mm



(b) Diameter: 10-16mm



(b) Diameter: 16-20mm

Fig.13 AE energy fractal dimension curves of combinations with 22mm-diameter waveguide rod

the approach of sliding failure. Therefore, the 1,000 samples of the last fractal dimension produced in a sliding phase is used to plus the truncated data. Meanwhile, considering the obvious AE phenomena during the sliding failure of slopes [18-19], the fractal dimensions of AE energy are averaged, i.e., all AE fractal dimensions are firstly grouped by a certain step-

size, and then the AE fractal dimensions of each step are averaged. The AE energy fractal dimension curves of the nine combinations are shown in Figs.11~13.

According to the energy fractal dimension curves, the AE energy fractal dimension remained at a low level in the initial phase. This means the AE energy fell into an orderly state.

As the test moved to the middle phases, the fractal dimensions continued to increase and reached its maximum, indicating that AE energy shifted from the orderly state to a chaotic state. In the final phase of the test, the fractal dimensions plunged suddenly. The sudden decrease not only reveals the restoration of the order in AE energy, but also marks the point that the fractal dimension peaked and then dived near the slip-impending phase. Consequently, the AE fractal dimension also peaked at the slip-impending phase and then drop all of a sudden. This could serve as a precursor of embankment slope failures.

5. Conclusions

In this paper, nine combinations of waveguide rods and gravels are obtained for an indoor similarity simulation of embankments. In the simulation tests, the AE feature data of the embankment slope models are obtained during the failure process. Then, the fractal theory is applied to analyse the features and variation patterns of the AE energy fractal dimensions of the embankment slopes throughout the failure process. The test results show that the fractal dimension remained at a low level at the onset, continued to increase during the test, and eventually peaked at the middle phase of the test. In the final phase, the fractal dimension started to decrease. The authors also analysed the features and variation patterns of AE energy fractal dimension during embankment slope failure, and discovered that the AE fractal dimension also peaked at the slip-impending phase and then drop all of a sudden. The results can serve as a precursor of embankment slope failures.

In the future, the authors will discuss why the AE peaked in the combinations with gravel particle size of 10~16mm, and performance quantitative analysis on the variation pattern of AE energy fractal dimension during the embankment slope failure.

Acknowledgments

The authors gratefully acknowledge the financial support from the Project supported by the National Natural Science foundation of China (No. 51504102, 51764014, 51404111), China Postdoctoral Science Foundation (No. 2017M622099), National key technologies Research and Development program (No. 2017YFC0804601), Program of Qingjiang Excellent Young Talents, Jiangxi University of Science and Technology.

References

1. Liu, J. X., Yang, C. H., Gan, J. J., Liu, Y. T., Wei, L. and Xie, Q. (2017): "Stability Analysis of Road Embankment Slope Subjected to Rainfall Considering Runoff-Unsaturated Seepage and Unsaturated Fluid-Solid Coupling." *International Journal of Civil Engineering*, vol. 15, no. 6, pp. 865-876, 2017.

2. Yuan, C., Yu, Q. H., You, Y. H. and Gou, L. (2017): "Deformation mechanism of an expressway embankment in warm and high ice content permafrost regions," *Applied Thermal Engineering*, vol. 121, pp. 1032-1039, 2017.
3. Hou, X. T., Wan, Y. H., Zhang, J. X. and Xiong, W. (2014): "Experimental study on prediction of landslide disaster based on AE," *Journal of China and Foreign Highway*, vol. 34, no. 1, pp. 36-39, 2014.
4. Zhong, W., Chen, X., Han, J. W., Wang, X. J., Zhao, K. and Tan, Z. Y. (2017): "Weathered slope stability analysis in open-pit mine based on weak interfaces exploration," *Electronic Journal of Geotechnical Engineering*, vol. 22, no. 8, pp. 2969-2980, 2017.
5. Khalilzad, M., Gabr, M. A., Hynes, M. E. (2015): "Assessment of remedial measures to reduce exceedance probability of performance limit states in embankment dams," *Computers and Geotechnics*, vol. 67, pp. 213-222, 2015.
6. Smethurst, J., Smith, A., Uhlemann, S., Uhlemann, S., Wooff, C., Chambers, J., Hughes, P., Lenart, S., Saroglou, H., Springman, S. M. and Lofroth, H. (2017): "Current and future role of instrumentation and monitoring in the performance of transport infrastructure slopes," *Quarterly Journal of Engineering Geology and Hydrogeology*, vol. 50, no. 3, pp. 271-286, 2017.
7. Hilarov, V. L. (2015): "Detection of the Deterministic Component in Acoustic Emission Signals from Mechanically Loaded Rock Samples," *Physics of the Solid State*, vol. 57, no. 11, pp. 2271-2278, 2015.
8. Iturrioz, I., Lacidogna, G. and Carpinteri, A. (2014): "Acoustic emission detection in concrete specimens: Experimental analysis and lattice model simulations," *International Journal of Damage Mechanics*, vol. 23, no. 3, pp. 327-358, 2014.
9. Gdawiec, K. (2017): "Fractal patterns from the dynamics of combined polynomial root finding methods," *Nonlinear Dynamics*, vol. 90, no. 4, pp. 2457-2479, 2017.
10. Mandelbrot, B. B. (1967): "How long is the coast of Britain, statistical self-similarity and fractal dimension," *Science*, vol. 156, pp. 636-638, 1967.
11. Gao, B. B., Li, H. G., Li, H. M., Li, L. and Su, C. D. (2015): "Acoustic emission and fractal characteristics of saturated coal samples in the failure process," *Journal of Mining and Safety Engineering*, vol. 32, no. 4, pp. 665-670+676, 2015.
12. Khosravizadeh, M., Dehestani, M. and Kalantary, F. (2016): "On the seismic stability and critical slip surface of reinforced slopes," *Soil Dynamics and Earthquake Engineering*, vol. 85, pp. 179-190, 2016.

Continued on page 443